

Anomalous electronic heat capacity of copper nanowires at sub-kelvin temperatures

K. L. Viisanen and J. P. Pekola

*Low Temperature Laboratory, Department of Applied Physics,
Aalto University School of Science, P.O. Box 13500, 00076 AALTO, Finland*

(Dated: March 1, 2018)

We have measured the electronic heat capacity of thin film nanowires of copper and silver at temperatures 0.1–0.3 K; the films were deposited by standard electron-beam evaporation. The specific heat of the Ag films of sub-100 nm thickness agrees with the bulk value and the free-electron estimate, whereas that of similar Cu films exceeds the corresponding reference values by one order of magnitude. The origin of the anomalously high heat capacity of copper films remains unknown for the moment. Based on the small heat capacity at low temperatures and the possibility to devise a tunnel probe thermometer on it, metal films form a promising absorber material, e.g., for micro-wave photon calorimetry.

I. INTRODUCTION

For improving the energy resolution of cryogenic bolometers and calorimeters, the thermal properties of mesoscopic structures play a key role. They can deviate significantly from the properties of bulk materials due to the surface effects that manifest in structures with a large surface-to-volume ratio. Breaking the periodic condition of a bulk material induces surface states and affects the bonding in the material, which can dramatically change its electric and magnetic properties by transforming conductors into insulators or semiconductors, and by inducing magnetism in materials that are non-magnetic in bulk. Anomalous behavior can also result from impurities, dislocations in the lattice, or from a natural oxide layer growing on the surface. Due to its good thermal, electrical and mechanical properties, copper is widely used in low temperature experiments for instance in thermometry, calorimetry and bolometry, development of electric current standards, refrigeration by nuclear demagnetization and electronic cooling^{1–9}.

For applications in calorimetry, the main characteristics of metals under interest are, in addition to the electric properties, the specific heat of the conduction electrons and their thermal coupling to the environment. Magnetic impurities of per mil concentration level are observed to enhance the specific heat of Cu by a few times at sub 1 K temperatures¹⁰ and the surface of Cu is proposed to host Kondo impurities¹¹ in the dephasing time measurements, which are sensitive to even a dilute magnetic impurity concentration, intensively studied in mesoscopic Cu structures during the last decades^{11,12}. The specific heat of an electron gas interacting with low concentration of randomly distributed magnetic impurities is determined by the Kondo temperature, T_K , in the material and can exceed the free electron specific heat by orders of magnitude¹³.

The surface of Cu structures is usually covered by its natural oxides. CuO is paramagnetic even in bulk and CuO₂ has been observed to exhibit various magnetic properties such as antiferromagnetism and ferromagnetism in nanoparticles, even though the bulk structure is diamagnetic^{14,15}. Theoretical analysis of Cu oxide

surfaces traces the origin of ferromagnetism in the pure CuO₂ nanoparticles to the increased 2p-3d hybridization in the nanomaterial, and the modelling of cation vacancies in an ideal CuO₂ crystal as well as on its surfaces indicates the vacancies to be a possible source of the observed magnetic moments^{15,16}. Cupric oxide layers play an important role also in the observed high transition temperature superconductivity of several heavy fermion compounds, where the effective mass can exceed that of bare electrons by two orders of magnitude resulting in significant increase in the specific heat of the compound¹⁷.

Lattice dislocations induce electric field gradients (EFG) in a material. Additional heat capacity arising from the nuclear spin coupling to the EFG created by crystal field distortions and magnetic impurities in metals has been discussed in Ref.¹⁸. Previous measurements in magnetic metallic calorimeters suggest that additional specific heat in Au arises from the nuclear quadrupole coupling to the EFG introduced by Er ions¹⁹. The accurate estimation of strain induced EFGs is in practice challenging, since each individual dislocation in the lattice should be included in the model.

II. DESCRIPTION OF THE EXPERIMENT

In this paper we present specific heat measurements at temperatures 120–250 mK of Ag and Cu thin film wires. The normal metal specific heat at low temperatures is given by $c = \gamma T + \beta T^3$, where the first term is due to the conduction electrons and the second one comes from the lattice phonons. At sub-kelvin temperatures, the phonons are frozen out and the electrons are left as the main source of heat capacity, whereas at higher temperatures, the electronic contribution is negligible. The specific heat measurements on bulk Cu and Ag address the sum of the two components^{20–23}. The literature values of the low temperature specific heat for bulk Cu are usually 30 % higher than the free-electron estimate, while Ag seems to be a manifestation of the free-electron theory. In those measurements, the electronic contribution is extracted based on the temperature dependence, whereas, in our setup, the electronic heat capacity is measured di-

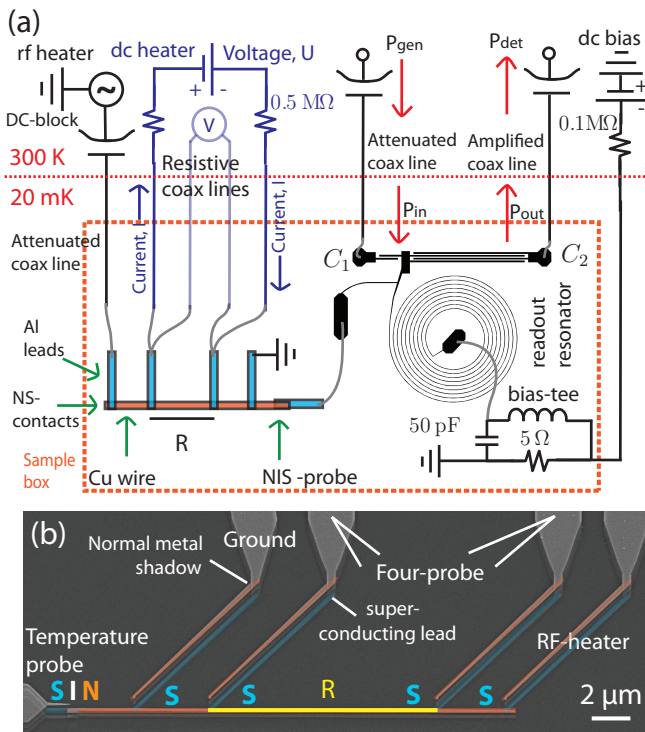


FIG. 1. The set-up of the measurements. (a) A schematic presentation. Four coaxial direct current (dc) wires are connected to the sample for calibrating the heating power. A dc bias is applied to the NIS-temperature probe through a bias-tee and a cold bias resistor at the printed circuit board (pcb) of the sample box. The thermometer is operated with an rf-drive, directed to the sample through a wide band coaxial wire. The readout is performed through a lumped element Al resonator, which is operated in a transmission mode. The coupling to the $Z_0 = 50 \Omega$ impedance transmission lines is realized with finger capacitors of capacitance $C_1 = 0.025$ pF and $C_2 = 0.22$ pF. The inductance of the spiral coil is 94 nH and the parasitic capacitance to ground from the resonator and the sample is 0.61 pF. Another rf-wire is connected to the sample to allow for the application of fast heating pulses. (b) Coloured micrograph of the sample for the heat capacity measurement. The resistance, R , is measured for the $12 \mu\text{m}$ long section of the actual wire, painted in yellow.

rectly as we Joule heat the electrons by electric current. We observe that Cu wires exhibit an anomalously large specific heat, exceeding the free-electron estimate by up to an order of magnitude, whereas the Ag wire follows the free-electron estimate.

The thin film samples were patterned by electron beam lithography and the metals were deposited using standard electron beam evaporation. We measure the temperature of the wires using a normal metal-insulator-superconductor (NIS) probe embedded in a lumped element tank circuit^{4,5,24,25}. A schematic illustration of the measurement setup and an image of the actual structure are shown in Fig. 1. The thermometer can detect temporal evolution of temperature down to μs time resolution in

TABLE I. Parameters of the samples and the resonators. The resistivities, ρ , of the metals are calculated from the measured R and the dimensions of the wires, given in Table II.

| Sample | Material | R (Ω) | ρ (Ωm) | R_T (k Ω) | Δ (meV) | R_0 (k Ω) | $\omega_0/2\pi$ (MHz) |
|--------|----------|------------------|-----------------------------|---------------------|----------------|---------------------|-----------------------|
| A | Cu | 96.9 | 3.3×10^{-8} | 29 | 2.16 | 34 | 550 |
| B | Cu | 18.6 | 3.0×10^{-8} | 21 | 2.38 | 33 | 563 |
| C | Ag | 80.5 | 3.2×10^{-8} | 11 | 2.12 | 45 | 552 |

mesoscopic metal structures, allowing the measurements of thermal relaxation rates and electronic heat capacities. In most cases the probe measures quasiparticle current of the junction⁴, but when placed near a superconductor, it can also operate as a Josephson thermometer²⁶ with lower dissipation. Upon optimization, the device is a promising candidate for microwave calorimetry, in which case the finite volume of the electron gas in the normal wire works as an absorber for incoming radiation. For a sensitive calorimeter, it is necessary to minimize the size of the wire, whereas for the present heat capacity measurement, this is not essential. The NIS-junction is connected to a 10 MHz bandwidth lumped element resonator with $\omega/2\pi = 0.5$ GHz resonance frequency, and it is operated here in the temperature range of 80–300 mK. The heat capacity, C_e , of the conduction electrons in the normal metal island is measured by heating the wire with a voltage pulse and probing the electron temperature, T_e , in the normal metal. The thermal response of the wire depends on the magnitude of the heating pulse, P_H , the heat conduction from the normal metal electrons to the environment, G_{th} , and C_e . All these quantities are deter-

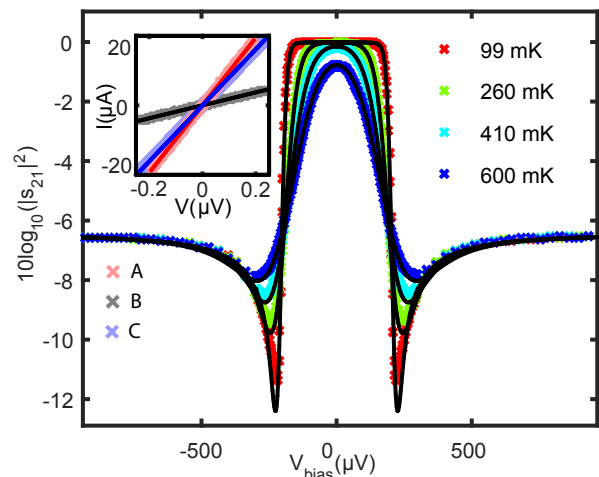


FIG. 2. Measured $|s_{21}|^2$ as a function of V_b in sample A. The theoretical estimates (black lines) are obtained with Eqs. (1) and (2), assuming T_e to be independent of V_b . This is a reasonable assumption for samples with large normal metal volume at biases $eV_b < \Delta$. In the top-panel, the current-voltage characteristics of the normal metal wires in samples A, B and C are shown. The solid lines are linear fits to the measured data.

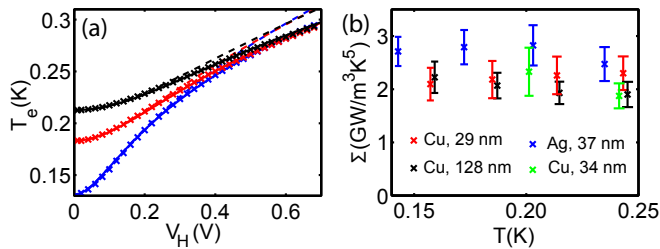


FIG. 3. Measurements of thermal coupling of the electrons in the wire to the bath. (a) Measured steady-state temperature T_e of sample A (28 nm thick Cu) against the amplitude of the continuously applied ac heating voltage at different bath temperatures. The solid lines are the theoretical estimates corresponding to $P_H + \dot{Q}_{ep} + \dot{Q}_{nis} + \dot{Q}_S = 0$, Σ and ρ_N ($\approx 2 \times 10^{-8} \Omega\text{m}$) are used as fitting parameters. The dashed lines are calculated by neglecting \dot{Q}_S , which is justified at temperatures below 250 mK. (b) The electron-phonon coupling constant, extracted for samples A-D, shown against bath temperature T .

mined separately in our measurement setup.

The heating power applied to the electron gas is determined in a four probe measurement, see Fig. 1. Two pairs of dc lines are connected to the island through direct NS-contacts. The resistance of the section of the wire between these contacts, R , is measured by applying dc current, I , through it and measuring the voltage, U , across it. The measurement data is shown in the sub-figure of Fig. 2. The linear slope in the IU -curve gives the resistance of the wire, see Table I. In the heat capacity measurement, the dc lines are left floating and the heating voltage, V_H , is applied through a low-pass filtered and attenuated rf-line. The magnitude of the rf heating is given by $P_H = AV_H^2$, where the constant A is determined by the attenuation in the heater line and the resistance of the normal wire. In practice, A is determined by comparing the response of T_e to the rf power and dc heating UI .

At resonance, the transmittance of voltage in the circuit can be written as

$$|s_{21}| = 2\kappa G_0 / (G + G_0), \quad (1)$$

where κ is about C_1/C_2 , $G_0 = Z_0(C_1^2 + C_2^2)\omega_0^2$ and $G = R_{nis}^{-1}$ is the differential conductance of the junction, given by

$$G = \frac{1}{k_B T_e R_T} \int_{-\infty}^{\infty} dE n_S(E) f(E - eV_b) (1 - f(E - eV_b)). \quad (2)$$

Here T_e is the electronic temperature in the normal metal, f is the Fermi function, $f(E) = [1 + \exp(-E/k_B T_e)]^{-1}$ and $n_S = n_0 |\text{Re}(E/\sqrt{E^2 - \Delta^2})|$ is the Bardeen-Cooper-Schrieffer density of states (DOS) of the superconductor, with n_0 the normal metal DOS at the Fermi level. The tunnelling resistances, R_T , of the NIS-junctions are measured in room temperature. The parameters of the resonators and the junctions are shown

in Table I. Typically, R_T increases by about 10%²⁷, when cooled down to sub-Kelvin temperatures. By measuring the $|s_{21}|^2$ vs V_b characteristics of the samples, one obtains an estimate for R_0/R_T . To determine R_0 , the values of R_T measured in room temperature, increased by 10%, are used. Fig. 2(b) shows the $|s_{21}|^2$ vs V_b characteristics measured in sample A at a few different bath temperatures. The superconducting gap is obtained by fitting to the data at base temperature.

III. THERMAL CONDUCTANCE MEASUREMENTS

The steady-state temperature on the normal metal island is governed by the heat balance $\dot{Q} + P_H = 0$. In the present configuration, \dot{Q} is given by $\dot{Q} = \dot{Q}_{ep} + \dot{Q}_{nis} + \dot{Q}_S + \dot{Q}_0$, where $\dot{Q}_{ep} = \Sigma \mathcal{V}(T^5 - T_e^5)$ is the power to the electron gas of the metal wire via electron-phonon scattering, \dot{Q}_{nis} is the heat carried by the tunnelling quasi-particles across the NIS-temperature probe and \dot{Q}_S is the heat leak across the superconducting aluminium leads. Here, Σ is a material-specific parameter to be discussed below, \mathcal{V} is the volume of the normal metal island and T is the temperature of the phonon bath. The background power from the environment to the island, \dot{Q}_0 , is assumed to be constant (at all bath temperatures), and we assume that T does not depend on the heating power. Due to \dot{Q}_0 , T_e of the carefully thermally isolated nanowire saturates to a value close to 100 mK even without external power. Since all the leads directly connected to the normal metal wire are superconducting, the heat flow along them is suppressed at low temperatures. For a superconducting wire of length l , thickness t and width w , \dot{Q}_S can be estimated at temperatures $k_B T_S \ll \Delta$ with $\dot{Q}_S \approx -\frac{wt}{l} \int_{T_S}^{T_e} dT' \kappa_S(T') e^{-\Delta/k_B T'}$,

where $\kappa_S(T') = \frac{6}{\pi^2} \frac{\mathcal{L}\Delta}{k_B \rho_N} \frac{\Delta}{k_B T'}$, \mathcal{L} is the Lorenz number and ρ_N is the normal state resistivity of the superconductor. In the present sample, there are four superconducting leads directly connected to the normal metal wire, each of them thermalized to T_e at the NS interface on the wire and to T at the intersection between the superconducting lead and the normal metal shadow. \dot{Q}_{nis} is given by $\dot{Q}_{nis} = \frac{1}{e^2 R_T} \int n_S(E) (E - eV_b) [f_N(E - eV_b) - f_S(E)] dE$. R_T and \mathcal{V} of the measured samples are sufficiently large, such that $\dot{Q}_{nis} \ll \dot{Q}_{ep}$, which allows us to extract Σ in the normal wire by measuring T_e under different heating powers, as shown in Fig. 3(a).

The electron-phonon coupling constant Σ is measured in samples A-D. The results are shown as a function of T in Fig. 3(b), and the average values are gathered in Table II. The parameters are determined by measuring the steady-state temperature under heating (samples A-C) and as a reference in a standard SINIS cooling experiment¹ using a DC measurement with four NIS tunnel junctions (sample D). The values mea-

sured in this work, $\Sigma \approx 2 \times 10^9 \text{ W/m}^3\text{K}^5$ for Cu and $\Sigma \approx 3 \times 10^9 \text{ W/m}^3\text{K}^5$ for Ag are in agreement with previously measured values for Cu²⁸. For Ag, there is less data found in literature, but an estimate of $0.5 \times 10^9 \text{ W/m}^3\text{K}^5$ was inferred by using Σ as a fitting parameter in an experiment of Ref.²⁹. For reference, rough theoretical estimates of Σ can be written with the density, ρ , the speed of sound, c , and the Fermi wave vector, k_F , in the metal as $\Sigma = \frac{\zeta(5)}{3\pi^2} \frac{k_F^4 k_B^5}{\hbar^3 c \rho}$, where $\zeta(5) \approx 1.0369$. For Ag and Cu, this would give values $\Sigma = 4 \times 10^8 \text{ W/m}^3\text{K}^5$ and $\Sigma = 2 \times 10^8 \text{ W/m}^3\text{K}^5$, respectively.

IV. HEAT CAPACITY MEASUREMENTS

We measure C_e of a normal metal wire by heating it with a voltage pulse of finite length and observing the time-dependent temperature T_e of the electron system. Its time evolution is determined by the heat balance equation

$$C_e \frac{dT_e}{dt} = \dot{Q} + P_H. \quad (3)$$

The measured T_e after switching on a sinusoidal 6 MHz heating pulse is shown in Fig. 4(a) as a function of time. Below $T = 250 \text{ mK}$, due to the suppressed heat flow across the superconducting leads, the heat exchange between the normal metal electrons and the environment occurs mainly through the electron-phonon scattering as was demonstrated in Fig. 3. Since Σ was measured independently in a DC measurement, C_e can then be determined accurately from the measured time traces. In particular, for small enough power, T_e decays exponentially back to equilibrium with the time constant $\tau = C_e/G_{\text{th}}$ after switching off the heating pulse, see Fig. 4(b). The thermal conductance is given by $G_{\text{th}} = -\frac{d\dot{Q}_{\text{ep}}}{dT_e} = 5\Sigma\mathcal{V}T_e^4$.

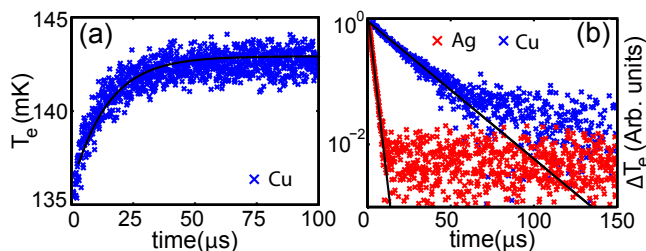


FIG. 4. Thermal relaxation measurements. (a) Time evolution of T_e in a thin Cu wire (sample A) after switching on the heating pulse. The black solid line is calculated by solving the heat balance equation (3). (b) Thermal relaxation of thin Cu (sample A) wire at $T = 107 \text{ mK}$ (blue) and Ag (sample C) wire at $T = 102 \text{ mK}$ (red) after switching off the heating. The quantity on the vertical axis, obtained by subtracting the background and normalizing the signal, is proportional to $\Delta T_e = T_e - T$. The solid lines are exponential fits to the data. The timetraces are obtained by averaging over 10^5 repetitions.

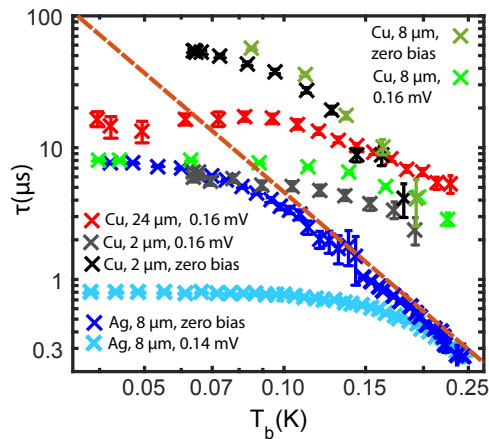


FIG. 5. Thermal relaxation time constants observed in a silver wire and three copper wires of different lengths. The dashed line shows the $\tau = \gamma/(5\Sigma T^3)$ dependence, using the free-electron Sommerfeld coefficient γ and the measured Σ of Ag ($\gamma/(5\Sigma) = 4.6 \times 10^{-9} \text{ sK}^3$). The decrease of the error bars in the Ag data at 150 mK is due to the increased averaging and larger heating amplitudes used at higher temperatures. The data measured at zero-bias indicates slower thermal relaxation both in Cu and Ag. This can be partly due to the enhanced heat transport via quasiparticle tunnelling compared with the electron-phonon heat current in the smaller samples. More probable explanation is, however, the saturation of T_e at low temperatures due to the noise induced by biasing the junction.

The heat capacity of the conduction electrons in a conventional metal can be estimated with the free-electron model as $C_e = \gamma\mathcal{V}T_e$, where $\gamma = \frac{\pi^2}{3} n_0 k_B^2$ is the Sommerfeld coefficient for the metal. For this ideal system, we thus expect the relaxation time to obey $\tau = \gamma/(5\Sigma T_e^3)$.

We have measured the thermal relaxation times of Cu and Ag wires at different bath temperatures, T . The thermal relaxation times after switching off the heating are obtained by fitting an exponential function to the measured data, from which the background is subtracted and the trace is normalized. There is a $\sim 2 \mu\text{s}$ electrical transient when switching the heating pulse on and off: data over this time is not included in the fits. In the Cu samples, the relaxation seems to consist of two time constants, whereas in the Ag samples, the relaxation can be fitted with a single exponent, τ , which is clearly faster than the time constants in Cu. This is the most direct evidence of the largely different specific heats of Ag and Cu wires, see Fig. 4(b). In Fig. 5, the thermal relaxation in Cu and Ag wires are shown as a function of T . The time constants shown for Cu are obtained with a two-exponent fit, while only the faster time constants are included in the plot. The slower relaxation observed in the Cu samples depends on the amplitude and the length of the heating pulse, increasing up to around $150 \mu\text{s}$ at large heating voltages. This relaxation is possibly related to an additional heat capacity, that relaxes slowly after switching off the heating pulse. When the heating pulse

is short and the temperature rise only a few mK, this effect is negligible. To rule out thermal gradients along the wire, we have measured the temperature relaxation in two additional Cu wires of lengths $8\ \mu\text{m}$ and $2\ \mu\text{m}$, see Fig. 5. By describing the thermal relaxation of the free electrons in the normal metal wire with the Wiedemann-Franz relation between the thermal and electrical conductivities, $\kappa/\sigma = LT_e$, where L is the Lorenz number, the response time of the electron temperature in the wire can be estimated as $\tau_{e-e} = C_e/\kappa_{\text{th}} = \gamma\rho l^2/L$. For the $24\ \mu\text{m}$ wires this results in about 50 ns, which is about three decades smaller than the timescales observed in the Cu wires. Due to the quadratic dependence on length, the relaxation in the $2\ \mu\text{m}$ wire should be over two decades faster compared with the $24\ \mu\text{m}$ wires, which is not observed in our measurements. From these perspectives we can rule out the possibility of significant thermal gradients along the wires.

The specific heat of samples A-C, measured at different bath temperatures, is shown in Fig. 6. The data are obtained by fitting the heat balance equation (3) to the measured time evolution of T_e after switching on a 6 MHz sinusoidal heating voltage, as illustrated in Fig. 4. Compared to the Cu wires, the thermal relaxation time of the Ag wire is clearly shorter, and hence its specific heat is lower. The results are similar to those obtained from the decay traces after switching off the pulse. In practice the fast relaxation means that the measurement in Ag wire is limited to temperatures well below 0.2 K because of the finite bandwidth of the thermometer. The largest specific heat is observed in the thin Cu wire. Especially with large amplitude heating pulses, an extra, very slow relaxation is observed in copper samples, which is evident in the non-exponential decay in Fig. 4(b) as well. Therefore, for the analysis of copper data, only the beginning of the trace, $\sim 1.5\tau$ after switching on the heating pulse, was included in the fits. Within the free-electron model, the Sommerfeld coefficient γ obtains values $\gamma = 70.7\ \text{J}/\text{m}^3\text{K}^2$ and $\gamma = 62.4\ \text{J}/\text{m}^3\text{K}^2$ for Cu and Ag, respectively. According to the data in Fig. 6, the Ag wire follows the free-electron theory, while an anomalously large specific heat is observed in the Cu wires. The specific heat of the thinner Cu wire exceeds the expectation value by an order of magnitude, while that of the thicker wire is somewhat lower. The temperature dependence in the two Cu samples is nearly quadratic, rather than linear predicted by the free-electron theory.

V. DETAILED CHARACTERIZATION OF THE SAMPLES

The measured samples are fabricated by electron-beam lithography and multi angle metal deposition in an electron-beam evaporator. In the evaporator, the samples are mounted on a room temperature platform in a vacuum chamber. During evaporation, the pressure in the chamber is between 1×10^{-7} mbar and

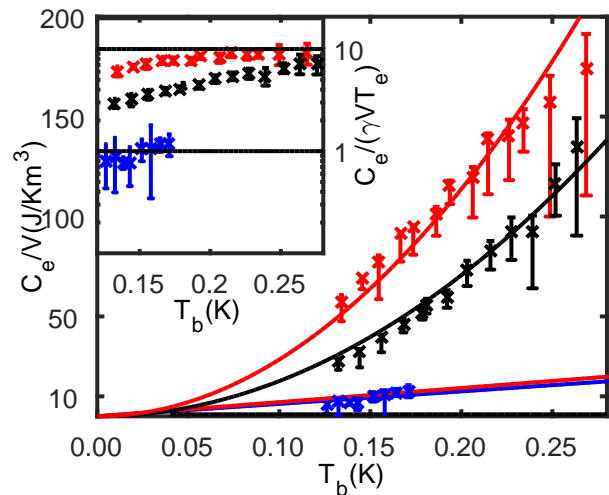


FIG. 6. Specific heat of the normal metal wires measured at different bath temperatures. The solid lines correspond to the free-electron estimate for Cu (red) and Ag (blue). The data for the Ag wire falls close to the free-electron estimate, while the specific heat of the Cu wires is clearly higher with rather a quadratic dependence on T (dashed lines). The normalized specific heat, $C_e/(\gamma V T)$, is shown as a function of T in the inset of the figure. Here γ is the Sommerfeld coefficient for each metal.

1×10^{-6} mbar and the growth rate of the film is in the range 0.1–0.3 nm/s. Typically the samples are stored in ambient air for a period ranging from hours to days before the cooldown to mK temperatures. We have observed, that the junction resistance of an Ag – AlO_2 – Al tunnel contact increases when stored in room temperature. Indeed, in about a day, the electrodes detach completely. We have found this to be a typical problem with the Ag samples, while the Cu – AlO_2 – Al tunnel junctions are more robust.

The geometry and the atomic composition of the samples are analyzed with scanning electron microscopy (SEM), atomic force microscopy (AFM), secondary ion mass spectroscopy (SIMS) and scanning transmission electron microscopy (STEM). The length and width of the wires are determined by SEM imaging, while the thickness is measured by AFM. These values are shown

TABLE II. Physical dimensions and the average values of Σ of the normal metal wires measured in this work. The resistances of the metals are measured for the $12\ \mu\text{m}$ long section of the $l = 24\ \mu\text{m}$ long wires.

| Sample | Material | l (μm) | w (nm) | t (nm) | ν (μm^3) | Σ ($\frac{\text{GW}}{\text{m}^3\text{K}^5}$) |
|--------|----------|--------------------------|--------------|-------------|------------------------------|--|
| A | Cu | 24 ± 0.1 | 145 ± 5 | 28 ± 1 | 0.10 ± 0.01 | 2.2 ± 0.2 |
| B | Cu | 24 ± 0.1 | 150 ± 10 | 128 ± 1 | 0.43 ± 0.03 | 2.0 ± 0.1 |
| C | Ag | 24 ± 0.1 | 125 ± 5 | 37 ± 2 | 0.11 ± 0.01 | 2.7 ± 0.3 |
| D | Cu | 7.2 ± 0.1 | 180 ± 10 | 34 ± 1 | 0.044 ± 0.004 | 2.1 ± 0.3 |

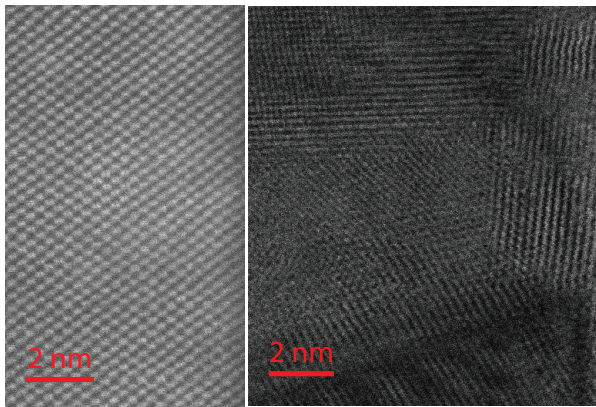


FIG. 7. STEM images of samples of (a) Ag and (b) Cu thin film nanowires. Several wires are imaged and all the Ag samples show a uniform lattice structure throughout the wire. The copper lattice, however, is formed of different growth directions, typical for evaporated Cu.

in Table. II.

The STEM imaging of the lattice structures is performed for 100 nm thick cross-sections of the wires, cut out by milling with focused ion beam (FIB). Before exposing to FIB, the samples are covered with a protective layer of Au. Several wires are measured and the lattice structure is found to be similar to that of bulk, no gas pockets or other anomalies are observed. The images are shown in Fig. 7. The lattice structure of the evaporated Ag wires is remarkably uniform; the lattice vectors point to the same direction throughout the wire. In the Cu wires, different growth directions are observed, which is typical for evaporated Cu films.

The amount of magnetic impurities in the evaporated metals is determined by SIMS, the level of 0.6 ppm is measured in Cu and 40 ppm in Ag³¹. The analysis is carried out for 50 nm thick films, fabricated on a similar substrate and deposited in the same evaporator as the measured samples. The Cu film fabricated of 99.9999 % pure source material was observed to be fairly clean with magnetic particles below the ppm level (Fe 0.2 ppm, Cr 0.02 ppm, Ni 0.2 ppm, V 0.004 ppm, Mn 0.01 ppm and Co 0.2 ppm). The Ag film deposited of 99.99 % pure starting material was observed to contain higher impurity levels (Fe 15 ppm, Cr 5 ppm, Ni 2 ppm, V 0.01 ppm, Mn 20 ppm and Co 0.08 ppm)³¹. The impurities in the source materials can also originate from the surface of the source material. Materials formed in a solution can result in lower surface contamination. This type of materials are coined "shot". By using 99.99 % shot Ag, 99.999 % shot Ag and 99.999 % Ag, we were able to reduce the level of Fe impurities below 3 ppm, but not lower. There was no significant difference in the observed impurity concentration of the metal films evaporated of these three source materials.

VI. SUMMARY AND OUTLOOK

In conclusion, we have measured thermal properties of thin Ag and Cu wires at sub-kelvin temperatures and observed an anomalously large specific heat in the Cu wires. Slow thermal relaxation in thin film Cu wires was previously reported in^{4,5}, whereas here we trace the long time constant to a large heat capacity, rather than small thermal conductance. The Ag samples are observed to follow the free-electron estimate, consistent with literature values measured in bulk. The band structures of Ag and Cu are similar, but the energies of the d-electrons are clearly lower in Ag³², which can explain why the free-electron model applies better for Ag. However, the observed anomaly in the electronic specific heat of Cu is much larger than that previously measured in bulk, exceeding the free-electron estimate by even an order of magnitude. The indication that the thicker wire would have lower specific heat suggests that the anomalously high specific heat could be related to the surface of the metal. However, more experiments are needed to confirm this conclusion. Magnetic impurities in Cu might increase the specific heat of the metal at low temperatures. At temperatures below T_K , the specific heat of an electron gas interacting with magnetic impurities is given by $c = k_B T / T_K$, which can be significantly larger than the free electron estimate. Around T_K , c develops a Kondo peak even at zero magnetic field, changing the power law of the specific heat¹³. Yet the concentration of known magnetic impurities in the evaporated Cu was measured to be as low as 0.6 ppm but 40 ppm in Ag. However, the natural Cu oxides, CuO₂ and CuO, are both magnetic, being a possible source of Kondo impurities in the measured samples. Another possible source of the enhanced specific heat can arise from the quadrupole splitting of the nuclei, due to the EFG generated by the distortion of the lattice¹⁹. The lattice of the evaporated Cu is imaged to have an irregular shape, whereas the Ag lattice is observed to be completely uniform. This would suggest the quadrupole splitting to be more likely to occur in the Cu samples. Fabricating much thicker Cu wires as well as wires with a passivated surface would provide valuable information for distinguishing between a surface effect and other possible sources of heat capacity. Further interesting measurements for understanding the phenomena now observed would be to explore a wider range of temperatures and looking at the dependence of the heat capacity on magnetic field. Based on our results, Ag exhibits a more promising candidate as an absorber material for a nanocalorimeter.

We acknowledge O.-P. Saira for the collaboration and discussions in the development of the RF-NIS thermometer, and A. Peltonen and H. Jiang for the chemical and structural analysis of the normal metal wires. J. Peltonen is acknowledged for contributing to the fabrication and design of the samples and M. Meschke for techni-

cal support with the measurement devices. We thank L. Wang, C. Enss, F. Hekking, H. Courtois, H. Pothier, J. Ankerhold, J. Ullom, Y. Galperin and M. Krusius for discussions. We acknowledge Jenny and Antti Wihuri

foundation and Academy of Finland projects 273827 and 285494 for financial support, and facilities and technical support provided by Otaniemi research infrastructure for Micro and Nanotechnologies (OtaNano).

-
- ¹ F. Giazotto, T. T. Heikkilä, A. Luukanen, A. M. Savin, and J. P. Pekola, *Rev. Mod. Phys.* **78**, 217 (2006).
- ² D. Rothfuß, A. Reiser, A. Fleischmann, and C. Enss, *Appl. Phys. Lett.* **103**, 052605 (2013).
- ³ D. J. Goldie, A. V. Velichko, D. M. Glowacka, and S. Withington, *J. Appl. Phys.* **109**, 084507 (2011).
- ⁴ S. Gasparinetti, K. L. Viisanen, O.-P. Saira, T. Faivre, M. Arzeo, M. Meschke, and J. P. Pekola, *Phys. Rev. Appl.* **3**, 014007 (2015).
- ⁵ K. L. Viisanen, S. Suomela, S. Gasparinetti, O.-P. Saira, J. Ankerhold, and J. P. Pekola, *New J. Phys.* **17**, 055014 (2015).
- ⁶ J. P. Pekola, O.-P. Saira, V. F. Maisi, A. Kemppinen, M. M. Möttönen, Y. A. Pashkin, and D. V. Averin, *Rev. Mod. Phys.* **85**, 1421 (2013).
- ⁷ I. Todoshchenko, J.-P. Kaikkonen, R. Blaauwgeers, P. J. Hakonen, and A. Savin, *Rev. Sci. Instrum.* **85**, 085106 (2014).
- ⁸ P. J. Lowell, G. C. O’Neil, J. M. Underwood, and J. N. Ullom, *Appl. Phys. Lett.* **102**, 082601 (2013).
- ⁹ H. Q. Nguyen, M. Meschke, and J. P. Pekola, *Appl. Phys. Lett.* **106**, 012601 (2015).
- ¹⁰ J. E. Jensen, R. B. Steward, H. Brencha, and A. G. Probell, *Selected cryogenic data notebook*, 1st ed. (Brookhaven National Laboratory, 1980).
- ¹¹ F. Pierre, A. B. Gougam, A. Anthore, H. Pothier, D. Esteve, and N. O. Birge, *Phys. Rev. B* **68**, 085413 (2003).
- ¹² J. Vranken, C. Van Haesendonck, and Y. Bruynseraede, *Phys. Rev. B* **37**, 8502 (1988).
- ¹³ J. Kondo, *Physics of dilute magnetic alloys* (Cambridge, U.K, 2012).
- ¹⁴ T. Ahmad, R. Chopra, K. Ramanujachary, S. Lofland, and A. Ganguli, *Solid State Sci.* **7**, 891 (2005), selected articles from the 4th International Conference on Inorganic Materials. Antwerp, Belgium 19-21 Septembre 2004.
- ¹⁵ C. Chen, L. He, L. Lai, H. Zhang, J. Lu, L. Guo, and Y. Li, *J. Phys. Condens. Matter* **21**, 145601 (2009).
- ¹⁶ X. Yu, X. Zhang, S. Wang, and G. Feng, *Curr. Appl. Phys.* **15**, 1303 (2015).
- ¹⁷ P. Coleman, *Heavy Fermions: Electrons at the Edge of Magnetism* (John Wiley & Sons, 2007).
- ¹⁸ K. Siemensmeyer and M. Z. Steiner, *Physik B - Condensed Matter* **89**, 305311 (1992).
- ¹⁹ C. Enss, A. Fleischmann, K. Horst, J. Schönfeld, J. Sollner, J. S. Adams, Y. H. Huang, Y. H. Kim, and G. M. Seidel, *J. Low. Temp. Phys.* **121**, 137 (2000).
- ²⁰ D. L. Martin, *Phys. Rev.* **170**, 650 (1968).
- ²¹ W. S. Corak, M. P. Garfunkel, C. B. Satterthwaite, and A. Wexler, *Phys. Rev.* **98**, 1699 (1955).
- ²² C. Kittel, *Introduction to Solid State Physics*, 7th ed. (John Wiley & Sons, 1996).
- ²³ F. Pobell, *Matter and Methods at Low Temperatures*, 3rd ed. (Springer, 2007).
- ²⁴ J. M. Rowell and D. C. Tsui, *Appl. Opt.* **14**, 2456 (1976).
- ²⁵ D. R. Schmidt, C. S. Yung, and A. N. Cleland, *Appl. Phys. Lett.* **83**, 1002 (2003).
- ²⁶ O.-P. Saira, M. Zgirski, K. L. Viisanen, D. S. Golubev, and J. P. Pekola, arXiv:1604.05089.
- ²⁷ K. Gloos, P. Koppinen, and J. Pekola, *Condens. Matter* **15**, 1733 (2003).
- ²⁸ M. Meschke, J. P. Pekola, R. E. Rapp, and H. Godfrin, *J. Low. Temp. Phys.* **134**, 1119 (2004).
- ²⁹ A. H. Steinbach, J. M. Martinis, and M. H. Devoret, *Phys. Rev. Lett.* **76**, 3806 (1996).
- ³⁰ F. C. Wellstood, C. Urbina, and J. Clarke, *Phys. Rev. B* **49**, 5942 (1994).
- ³¹ S. C. Kadia, “Evans analytical group,” (2015).
- ³² C. N. Berglund, *Band structure and electron-electron interactions in Copper and Silver—photoemission studies* (Stanford University, 1964).